Thermomechanical Modeling of Beam Blank Casting

Computational models of the mold and steel shell have been developed to investigate mold taper, gap formation, crack formation, and the effects of mold distortion and oscillation during beam blank casting. The models have been validated with plant measurements.

The continuous casting of near-net-shape cross-sections, called "beam blanks" or "dogbones," has been an efficient commercial process to manufacture long steel products such as I-beams since the first beam blank caster was installed at Algoma Steel (now Essar Steel Algoma Inc., Sault Ste. Marie, Canada) more than three decades ago. Its economic advantages over conventional bloom casting are due to higher productivity, lower rolling costs and improved energy efficiency.

The efficiency and quality of continuous cast steel is constantly improving, owing to increased automation and advances gained mainly through plant experimentation. However, empirical solutions are now very expensive without the aid of tools such as computational modeling. Practical applications of mathematical models include the design of mold geometry to control mold temperature and gap formation in order to avoid crack formation in both the mold and solidifying steel shell. In particular, the development of mold tapers to match the steel shrinkage is an ongoing challenge that must be met for each new cross-section, mold design and steel grade.

Defects arise if the mold has either too little or too much taper.[7–8] If any part of the internal mold shape has insufficient taper, gaps can open up between the solidifying steel shell and the mold wall, which drop the local heat transfer and lead to locally hot and thin sections. Combined with the ferrostatic pressure from the internal liquid pool, this can cause transverse strains on the newly solidified shell, which concentrate at the thin spots, resulting in longitudinal cracks or breakouts. Alternatively, if the mold taper is excessive anywhere, the mold pushes on the shell, leading to severe mold wear and/or buckling of the shell, and again leading to longitudinal cracks or breakouts. In addition, axial stresses from the mold friction can cause excessive local cooling and binding of the shell in the mold, generating transverse cracks and other problems.

Clearly there exists a strong incentive to develop quantitative computational models that can predict temperature, deformation and stress in the solidifying steel shell in the mold during continuous casting of near-net-shape sections with sufficient accuracy to solve practical problems such as the design of mold taper. Many computational models have been developed of thermal and mechanical behavior during continuous casting of steel.[2,5–6] Only a few previous models of the beam blank casting process have been attempted, owing to the computational difficulties associated with complex geometry and behavior.

Lait and Brimacombe pioneered the application of solidification models to beam blank casters. The predictions of their one-dimensional (1-D) moving-slice model compared well with plant measurements, but variations around the perimeter were not investigated.[9] Thomas and coworkers applied a two-dimensional (2-D) model of mold heat transfer to investigate water channel design in a beam blank mold, and identified how the concave internal-corner region where the web intersects the flange is susceptible to overheating and hot face cracks in the meniscus region of the mold.[10] Researchers at Voest-Alpine Industrial Services have used a 2-D transient finite-element model of heat transfer and stress in a horizontal slice through both the shell and mold to gain insights into beam

Authors

Lance C. Hibbeler (top), **Kun Xu** and **Brian G. Thomas** (bottom left), University of Illinois at Urbana-Champaign, Urbana, Ill. (lhibbel2@uiuc.edu, kunxu2@uiuc.edu, bgthomas@uiuc.edu); **Seid Koric** (bottom right), engineering applications analyst and technical coordinator for industrial projects, National Center for Supercomputing Applications (NCSA), Urbana, Ill. (skoric@ncsa.uiuc.edu); and **Clayton Spangler**, Steel Dynamics Inc. Structural and Rail Mill, Columbia City, Ind. (clayton.spangler@stld-cci.com)

blank mold design and shell behavior, but details are not provided.[11] Lee and coworkers showcased multiphysics modeling by coupling a three-dimensional (3-D) finite-difference model of fluid flow with a similar 2-D transient thermal-stress model to predict solidification, gap formation stress, and crack formation in a beam blank caster.[12] Impingement of steel flow from the nozzle inlet was found to retard shell solidification in the central regions of the flange (narrow face) and the web. Air gaps due to solidification shrinkage were predicted near the flange-tip corner. Surface cracks in the web and fillet regions and internal cracks in the flange-tip region were predicted. None of these predictions were checked with plant measurements.

The current study was undertaken to develop a thermomechanical model of the solidifying steel shell in the beam blank casting mold, using realistic boundary conditions and material properties. Furthermore, the model predictions are compared with plant measurements, in order to demonstrate sufficient accuracy for the optimization of mold taper.

Model Description

The computational model solves the coupled temperature, stress and deformation equilibrium equations in a beam blank caster. Separate models simulate thermal distortion of the mold, including the complete complex three-dimensional geometry of the copper plates and water box, and thermomechanical behavior of the solidifying steel shell, as it moves down through the mold. The latter "shell" model is fully coupled, as the heat transfer calculation depends on the air gaps computed with the mechanical model. Furthermore, the shell model is coupled with the 3-D "mold" model through the distorted shape of the wide-face and narrow-face surfaces, which are input as contact boundary conditions. Although the shell model produces complete steady-state results in three dimensions, the domain adopted for this work is a 2-D transient slice that moves down the mold at the casting speed. This popular Lagrangian approach has been used successfully in many previous solidification stress models.[5–6,13–14] This model alternates between solving the transient energy equation and the small-strain thermomechanical equilibrium equations, which are fully described in previous work.[2] Cracks will form if the strains exceed only a few percent, so the model can be accurately applied to investigate the initiation of crack formation using damage criteria. Total strain, $\dot{\varepsilon}$, in this elastic-viscoplastic model is divided into three components using a unified isotropic rate formulation to model the constitutive behavior:

$$\dot{\varepsilon} = \dot{\varepsilon}_{el} + \dot{\varepsilon}_{ie} + \dot{\varepsilon}_{th} \qquad \text{(Eq. 1)}$$

where $\dot{\varepsilon}_{el}$, $\dot{\varepsilon}_{ie}$, and $\dot{\varepsilon}_{th}$ are the elastic, inelastic (plastic + creep) and thermal strain rate tensors, respectively. Thermal strains arise due to volume changes caused by both temperature differences and phase transformations, and include the effect of solidification and solid-state phase transformations between crystal structures, using a simple mixture rule to linearly combine separate functions for liquid, delta-ferrite and austenite according to the phase fractions.

Constitutive Model — The inelastic (viscoplastic) strain component includes both strain-rate-independent plasticity and time-dependent creep. Creep is significant at the high temperatures of the solidification processes and is indistinguishable from plastic strain.[5] This work solves separate unified constitutive models for the austenite and delta-ferrite phases, which have been shown in previous work to accurately reproduce the temperature-, strain-rate- and composition-dependent behavior of solidifying steel.[5–6] For the austenite phase, it adopts model III from Kozlowski et al.[15] to relate equivalent inelastic strain rate $\dot{\bar{\varepsilon}}_{ie}$, von Mises stress $\bar{\sigma}$, temperature (in Kelvin), equivalent inelastic strain, an activation constant Q, and several temperature- or carbon-content-dependent empirical constants f_1, f_2, f_3 and f_C. This relation was developed to match both the tensile test measurements of Wray[21] and creep test data of Suzuki,[22] and is given in Equation 2. For the delta-ferrite phase, it adopts the Zhu power-law model,[6] given in Equation 3, which exhibits much higher creep rates than austenite. This power-law model has temperature- or composition-dependent constants $f_{\delta C}$, m, and n and is applied in the solid whenever the volume fraction of delta-ferrite is more than 10%. This approximates the dominating influence of the very high creep rates in the delta-ferrite phase of mixed-phase

Equation 2

Kozlowski Model III for Austenite:

$$\dot{\bar{\varepsilon}}_{ie}\left[\sec^{-1}\right] = f_C\left(\bar{\sigma}[MPa] - f_1\bar{\varepsilon}_{ie}\left|\bar{\varepsilon}_{ie}\right|^{f_2-1}\right)^{f_2}\exp\left(-\frac{Q}{T[K]}\right)$$

where

$Q = 44{,}465$,

$f_1 = 130.5–5.128 \times 10^{-3}T$ [K],

$f_2 = -0.6289 + 1.114 \times 10^{-3}T$ [K],

$f_3 = 8.132–1.54 \times 10^{-3}T$ [K] and

$f_C = 46{,}550 + 71{,}400$ (%C) $+ 12{,}000$ (%C)^2.

Equation 3

Zhu Power-Law Model for Delta-Ferrite:

$$\dot{\bar{\varepsilon}}_{ie}\left[\sec^{-1}\right]=0.1\left|\frac{\bar{\sigma}\left[MPa\right]}{f_{\delta c}\left(\%C\right)\left(\frac{T\left[K\right]}{300}\right)^{-5.52}\left(1+1{,}000\bar{\varepsilon}_{ie}\right)^{m}}\right|$$

where

$f_{\delta c}\,(\%C) = 1.3678 \text{ x } 10^{4}\ (\%\mathrm{C})^{-5.56 \text{ x } 10^{-2}}$,

$m = -9.4156 \text{ x } 10^{-5}\mathrm{T}\ [\mathrm{K}] + 0.3495$ and

$$n=\frac{1}{1.617\times10^{-4}T\left[K\right]-0.06166}.$$

structures on the net mechanical behavior. The calculation of the volume fractions of the liquid, delta and austenite phases proceeds according to the non-equilibrium phase diagram.[5,25–26] A typical example of the phase fractions is given in Figure 1 for the 0.07%C alloy used in this work.

The great variation in material properties between liquid, mush and solid creates a significant numerical challenge to accurate thermomechanical simulations, as discussed elsewhere.[2] In the current model, elements that contain both liquid and solid are generally given no special treatment regarding either material properties or finite element assembly. The only difference is to choose an isotropic elastic-perfectly-plastic rate-independent constitutive model that enforces negligible liquid strength when the temperature is above the solidus temperature:

$$\Delta\bar{\varepsilon}_{ie}^{t+\Delta t}=\frac{\bar{\sigma}^{*t+\Delta t}-\sigma_{Y}}{3\mu} \qquad \text{(Eq. 4)}$$

where

$\bar{\sigma}^{*t+\Delta t}$ = the von Mises elastic predictor and
μ = the shear modulus.

This simple fixed-grid approach avoids difficulties of adaptive meshing or "giving birth" to solid elements, such as used in Ansys.[16] Liquid or mushy elements are defined when $T > T_{sol}$ for at least one material (Gauss quadrature) point. The yield stress σ_y = 0.01 MPa is chosen small enough to effectively eliminate stresses in the liquid-mushy zones, but also large enough to avoid computational difficulties.

Owing to the highly strain-rate-dependent inelastic responses, a robust integration scheme is required to integrate the viscoplastic equations over a generic time increment Δt. The system of ordinary differential equations defined at each material point by the viscoplatic model (Equation 2, 3 or 4) is converted into two "integrated" scalar equations by the backward Euler method, and then solved using a special bounded Newton-Raphson method. Details of this local integration scheme can be found elsewhere,[2–3,5–6,17] along with the derivation of the consistent tangent operator ("material Jacobian") used with this method. Liquid and mushy elements are evaluated using the standard radial-return algorithm, which is a special form of backward-Euler procedure.[18–19] The algebraic equations associated with integrating the model are developed based on a single variable, the equivalent inelastic strain increment $\Delta\bar{\varepsilon}_{ie}$. These constitutive equations are implemented into the commercial finite element package ABAQUS[1] via its user-defined material subroutine UMAT. The solution obtained from this "local" integration step from all material points is used to update the global finite-element equilibrium equations, which are solved using the Newton-Raphson-based nonlinear finite-element procedures in ABAQUS. The Newton-Raphson method used in the global equilibrium equation iterations yields a quadratic convergence rate.[20]

Temperature-dependent properties were chosen for the 0.071%C plain carbon steel alloy with T_{sol} = 1,471.9°C and T_{liq} = 1,518.7°C (pour temperature of 1,523.7°C). Figure 1 shows the fractions of liquid and solid phases for this steel.[5] The variations with temperature of enthalpy, thermal conductivity, coefficient of thermal expansion, and elastic modulus for this steel grade were determined with empirical models described elsewhere.[2]

Interface Boundary Conditions — Heat transfer across the interfacial gap between the shell and the mold wall surfaces is defined with a resistor model that depends on the thickness of gap calculated by the stress model. Heat transfer occurs in two parallel paths, due to radiation, h_{rad}, and conduction, h_c, as follows:

$$q''_{gap}=-h_{T}\left(T_{shell}-T_{mold}\right)=-\left(h_{c}+h_{rad}\right)\left(T_{shell}-T_{mold}\right) \qquad \text{(Eq. 5)}$$

The radiation heat transfer coefficient h_{rad} is calculated across the transparent liquid portion of the mold slag layer:

$$h_{rad}=\frac{5.67\times10^{-8}}{\frac{1}{\varepsilon_{m}}+\frac{1}{\varepsilon_{s}}-1}\left(T_{shell}-T_{mold}\right)\left(T_{shell}^{2}+T_{mold}^{2}\right) \qquad \text{(Eq. 6)}$$

where

$\varepsilon_m = \varepsilon_s$ = 0.8 are the emissivities of the mold and shell surface, and

T_{mold} and T_{shell} are their current temperatures, respectively.

The conduction heat transfer coefficient, h_c, depends on four resistances connected in series:

$$\frac{1}{h_c} = \frac{1}{h_{mold}} + \frac{d_{air}}{k_{air}} + \frac{d_{pow}}{k_{pow}} + \frac{1}{h_{shell}} \quad \text{(Eq. 7)}$$

The first resistance, $1/h_{mold}$, is the contact resistance between mold wall surface and the solidified mold slag film. The contact heat transfer coefficient h_{mold} is chosen to be 2,500 W/m^2.[23] The second resistance, d_{air}/k_{air}, is conduction across the air gap, assuming $k_{air} = 0.06$ W/mK. The thickness of air gap, d_{air}, is determined from the difference between mold and shell displacements, calculated from the mechanical contact analysis, and the slag film thickness. An artificial constant slag film thickness, $d_{pow} = 0.1$mm, is adopted to prevent non-physical behavior associated with very small gaps.[23] The third resistance, d_{pow}/k_{pow}, is conduction through the slag film, assuming $k_{pow} = 1$ W/mK. The final term, $1/h_{shell}$, is the contact resistance between the slag film and the strand, where the shell contact heat transfer h_{shell} coefficient depends greatly on temperature. This shell-slag contact coefficient decreases greatly as the shell surface temperature drops below the solidification temperature of the mold slag.[24] The temperature dependency of h_{shell} is given in Table 1. These equations were implemented into ABAQUS using the user-defined subroutine, GAPCON.[1]

The internal ferrostatic pressure from the molten steel pushes the shell toward the mold and is modeled with a linearly increasing distributed load defined in Equation 8 that is applied to the shell contact surface starting at zero time at the meniscus:

$$F_p = -\rho g z \quad \text{(Eq. 8)}$$

where

ρ = density,
$g = 9.81$ m/s^2 is gravitational acceleration and
z = the current distance below the meniscus, which is easily calculated from the current time and the casting speed.

Sometimes the start of pressure application is delayed until the outermost layer of elements is solid, in order to avoid convergence problems.

Mechanical contact is applied between mold and strand contact surfaces, based on the mold surface location defined from the mold model results and the applied taper.

Figure 1

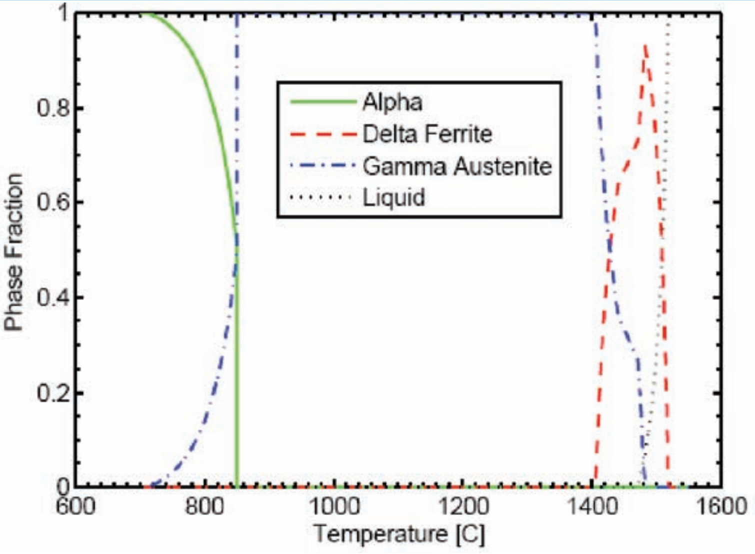

Phase fractions for 0.071%C plain carbon steel.

Table 1

Temperature Dependence of h_{shell}[24]

Temperature, °C	h_{shell}, W/m^{2}K
1,030	1,000
1,150	2,000
1,518	10,000
1,530	20,000

In this simulation, the mold is the "master" surface and the shell surface is the "slave" surface. Owing to the low strength of the shell at early times, an exponential softened contact algorithm[1] was required to enable convergence. This general model has been applied to simulate thermomechanical behavior in a wide range of continuous casting molds, including billets, slabs, thin-slab funnel molds and beam blanks.

Beam Blank Caster Specifics — Figure 2 shows a top view of the beam blank casting mold looking in the casting direction. The model simulated a BB2 beam blank with final cross-section dimensions of 555 mm (width) by 420 mm (flange thickness) by 90 mm (web thickness). Note that the mold dimensions given in the figure at the meniscus are slightly larger, in order to accommodate shrinkage of shell. The side view (Figure 3) shows that the mold is curved, which causes different temperature variations down the inside and outside radii. The finite element domain of the shell (Figure 4) is "snake" shaped, encompasses one-quarter of the shell section, and is wide

Figure 2

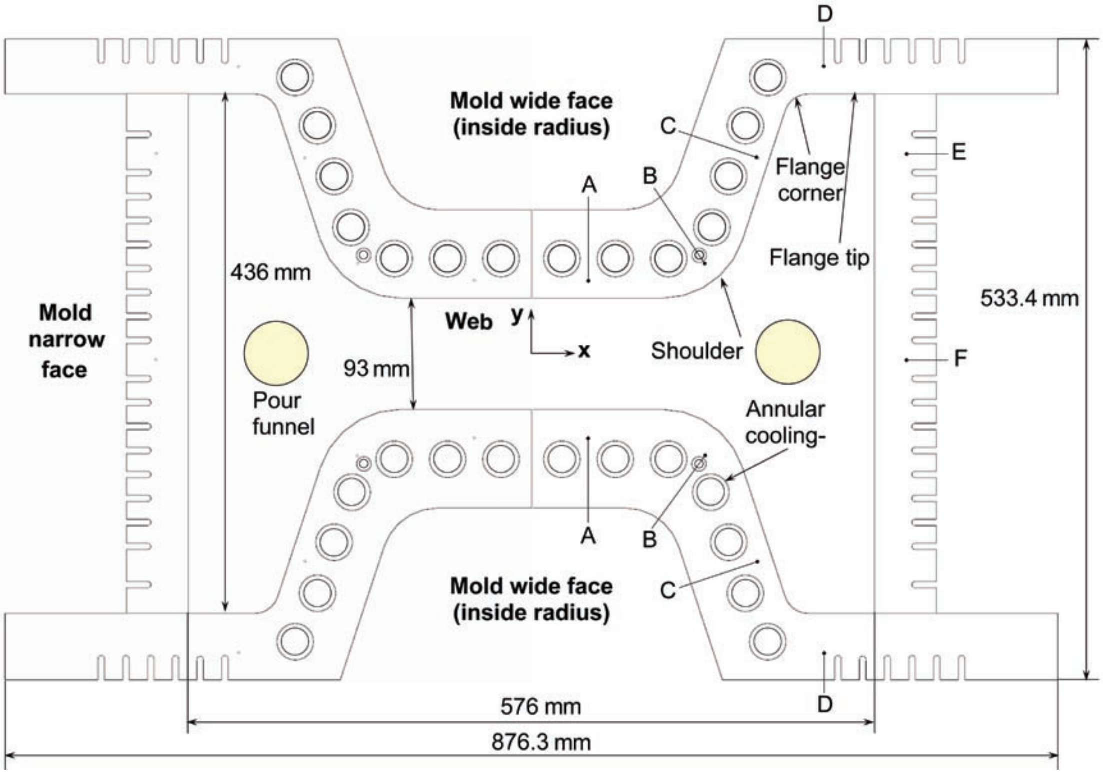

Horizontal plane mold geometry.

enough to allow solidification of the expected shell thickness everywhere. Temperature of the mold surface is approximated by simulating a simplified thin portion of the mold wall that extends up to, but not including, the water channels. This domain avoids expensive computation in the large, uninteresting liquid domain. More importantly, the shell is able to contract or expand around the missing internal core of liquid, which mimics the flow of liquid into and out of the plane, and greatly increases the robustness of the model. This behavior is not possible in a full one-quarter section domain.

The outer surface of the domain represents the mold and was modeled in three different ways. First, sections through the mold were modeled according to the actual geometry, shown in Figures 2 and 3. This domain includes the circular water slots, and

Figure 3

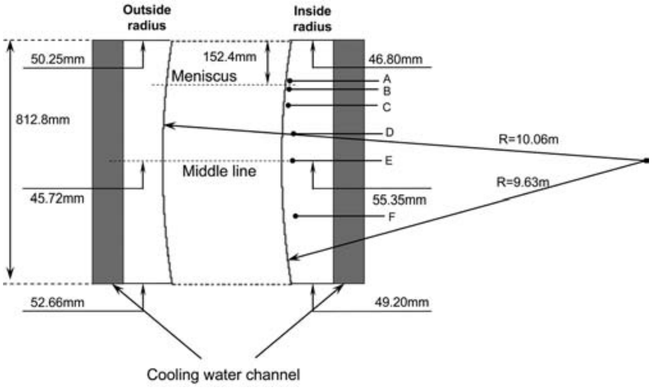

Schematic of beam blank caster and locations of thermocouples.

Figure 4

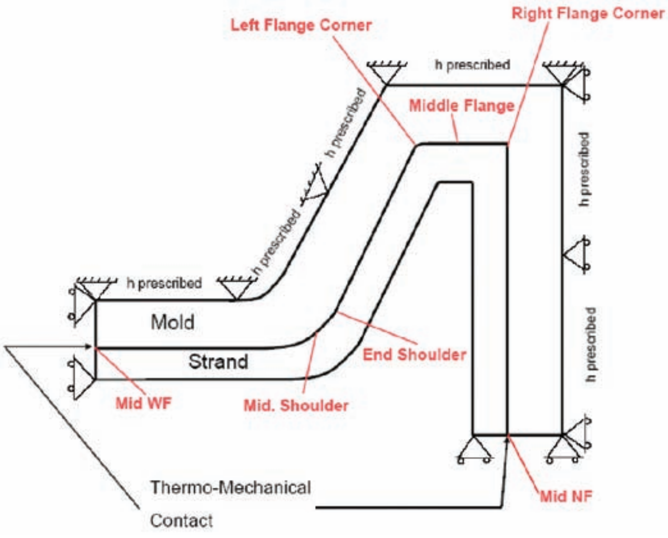

Shell modeling domain with thermomechanical boundary conditions.

the variation in mold copper thickness with distance down the mold, according to the machine curvature of about 10 m. This model was used in predicting realistic mold temperatures, in order to calibrate the coefficients in the model of heat conduction across the interfacial gap. Next, the mold model was simplified to the geometry given in Figure 4, by setting the outside domain to a line passing tangential to the circular water channels. This simplified model was used in modeling thermomechanical behavior of the solidifying shell. Finally, the complete three-dimensional mold was modeled, including the water slots, curved surfaces, and curvature of the water slots at the top and bottom of the mold. In all cases, the mold copper has a thermal conductivity of 370 W/mK and initial temperature of 285°C. The convection coefficients of h = 45 kW/m^{2}K transferring the heat from wide face surface to the cooling water with 33.35°C, and h = 34 kW/m^{2}K with 34.48°C on the narrow face are imposed on the portions of the outer mold surface matching the positions of cooling channels.

Thermal distortion and taper of the mold walls is incorporated by prescribing the displacements of the mold wall contact surfaces with respect to the time below meniscus. The taper in the beam blank mold in this work increases parabolically with distance down the mold, i.e., with higher taper gradients close to the meniscus and lower toward the mold exit, to better match the shell shrinkage history. The taper at mold exit relative to the meniscus is 0.48, 2.22, 2.33 and 3.00 mm on the web, shoulder, flange and narrow face, respectively. The casting speed is 0.889 m/minute, so the domain takes about 44.6 seconds to travel through the 660.4-mm working mold length.

The structured mesh for the beam blank shell has 9,000 four-node generalized plane strain elements using a hybrid formulation (one extra degree of freedom per element for pressure stress), with average size of 1.3 mm in the strand and 5 mm in the mold. The total number of degrees of freedom is over 40,000. ABAQUS required about 20 hours to finish this simulation on NCSA's Linux cluster of 3.2 GHz Intel Xeon processors.

Numerical Validation

The solidification stress model used in this work was first validated by comparison with the semi-analytical solution of the benchmark problem of thermal stress in an unconstrained solidifying plate, derived by Weiner and Boley[4] and with a previous finite-element model, CON2-D. A 1-D model of this test casting can produce the complete 3-D stress and strain state if the condition of generalized plane strain[5] is imposed in both the width (y) and length (z) directions. The domain adopted for this problem moves with the strand in a Langrangian frame of reference, as shown in Figure 5. The domain consists of a thin slice through the plate thickness using 2-D generalized plane strain elements (in the axial z-direction) implemented in ABAQUS. The second generalized plane strain condition was imposed in the y-direction (parallel to the surface) by coupling the displacements of all nodes along the bottom edge of the slice domain. The material in this problem has elastic-perfectly-plastic constitutive behavior. A very narrow mushy region, 0.1°C, is used to approximate the single melting temperature assumed by Boley and Weiner. The yield stress drops linearly with temperature from 20 MPa at 1,000°C to zero (approximated numerically as σ_y = 0.03 MPa) at the solidus temperature of 1,494.4°C.

Figure 5

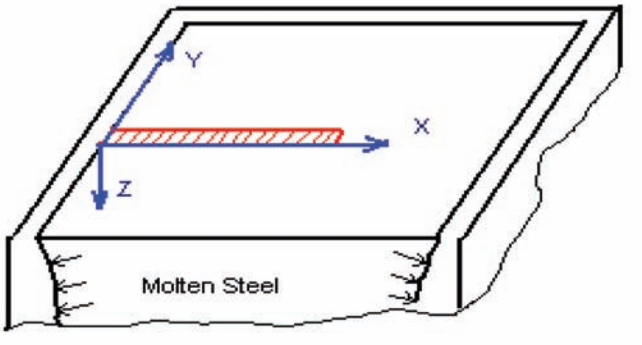

Solidifying slice.

Table 2

Constants Used in Solidification Test Problem

Conductivity [W/mK]	33.0
Specific heat [J/kg K]	661.0
Elastic modulus in solid [GPa]	40.0
Elastic modulus in liquid [GPa]	14.0
Thermal linear expansion coefficient [1/K]	0.00002
Density [kg/m^3]	7,500
Poisson's ratio	0.3
Liquidus temperature [°C]	1,494.45
Fusion temperature (analytical) [°C]	1,494.4
Solidus temperature [°C]	1,494.35
Initial temperature [°C]	1,495.0
Latent heat [J/kg K]	272,000.0
Reciprocal of liquid viscosity [MPa^{-1}sec^{-1}]	1.5 x 10^8
Surface film coefficient [W/m^{2}K]	250,000

Figure 6

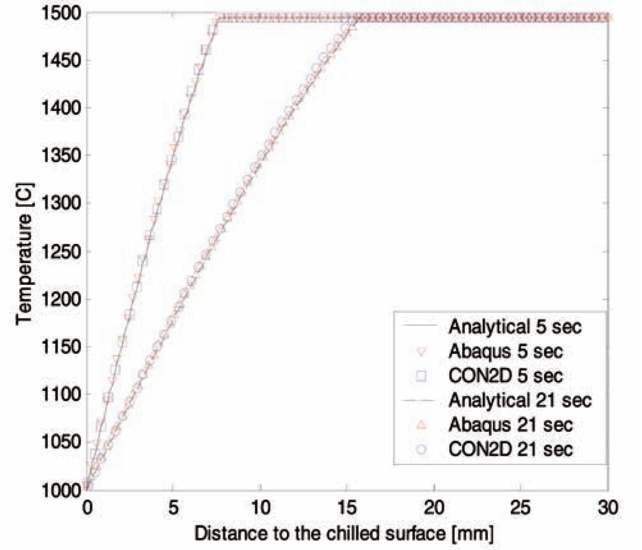

Temperature distribution along the solidifying slice.

Figure 7

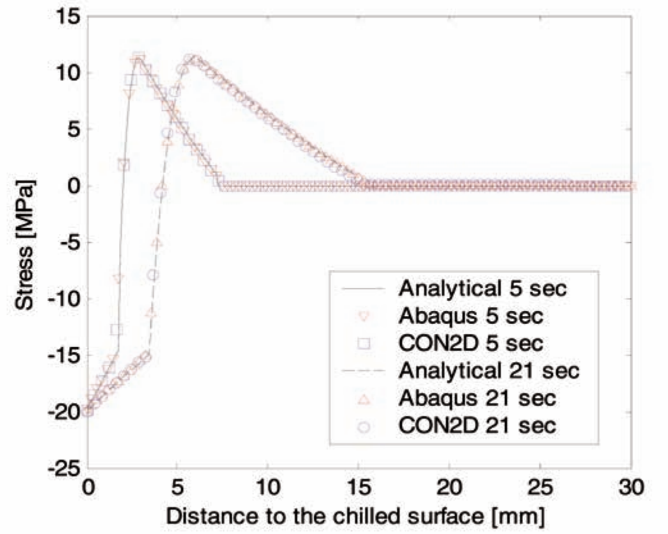

Stress distributions y and z along the solidifying slice.

Figures 6 and 7 show the temperature and the stress distribution across the solidifying shell at two different solidification times. These figures also include the solution to this problem from an in-house code, CON2-D.[5–6] Further comparisons with CON2-D for 2-D test problems also produced reasonable agreement. More details about this model validation can be found elsewhere,[2–3] including comparisons with other less-efficient integration methods and a convergence study, which shows that the shell with element sizes of approximately 1.3 mm on the chilled surface gradually increased to 3 mm deep in the liquid/mushy zone and was still able to reproduce reasonable temperature and stress results (within 5% error).

Plant Measurements

A BB2 beam blank mold at Steel Dynamics in Columbus City, Ind., was instrumented with 47 thermocouples, as located in Figures 2 and 3. Temperatures were collected during the continuous casting of 0.071 %C low-carbon A992 structural steel with casting speed at 0.889 m/minute. The Si-Mn-killed steel was open-poured into two ceramic funnels, located in the central flange regions, as shown in Figure 2. Mold temperatures were averaged over 30 minutes of casting. The chromel-slumel K-type thermocouples were inserted into holes drilled through the copper. Although the fit was very tight, thermal paste was not used, so thermal distortion was able to create small gaps (on the order of 0.01 mm) between the thermocouple tip and the root of each drilled hole. Heat conduction along the thermocouple wire caused the recorded temperatures to drop, especially for the thermocouples that extended directly through the center of the round water channels, such as thermocouple B in Figure 2.

Figure 8

Photograph of breakout shell.

The total rate of heat removal to the cooling water was measured to be 1,112.4 kW to the wide face, and 651.4 kW to the narrow face. During continuous casting under similar conditions, a breakout occurred, due to thinning and failure at the concave shoulder just below mold exit. Figure 8 shows the breakout shell, which provided a rare opportunity to further validate the computational model. The shell thickness was measured both down the mold narrow face (50 mm from the corner) and around the perimeter (at 457 mm below meniscus).

Model Calibration

The accurate 2-D slice model of the mold was used to calibrate the heat flux profile to simultaneously match the temperature measurements on both inside and outside radii at various cross-sections, in addition to the total

Figure 9

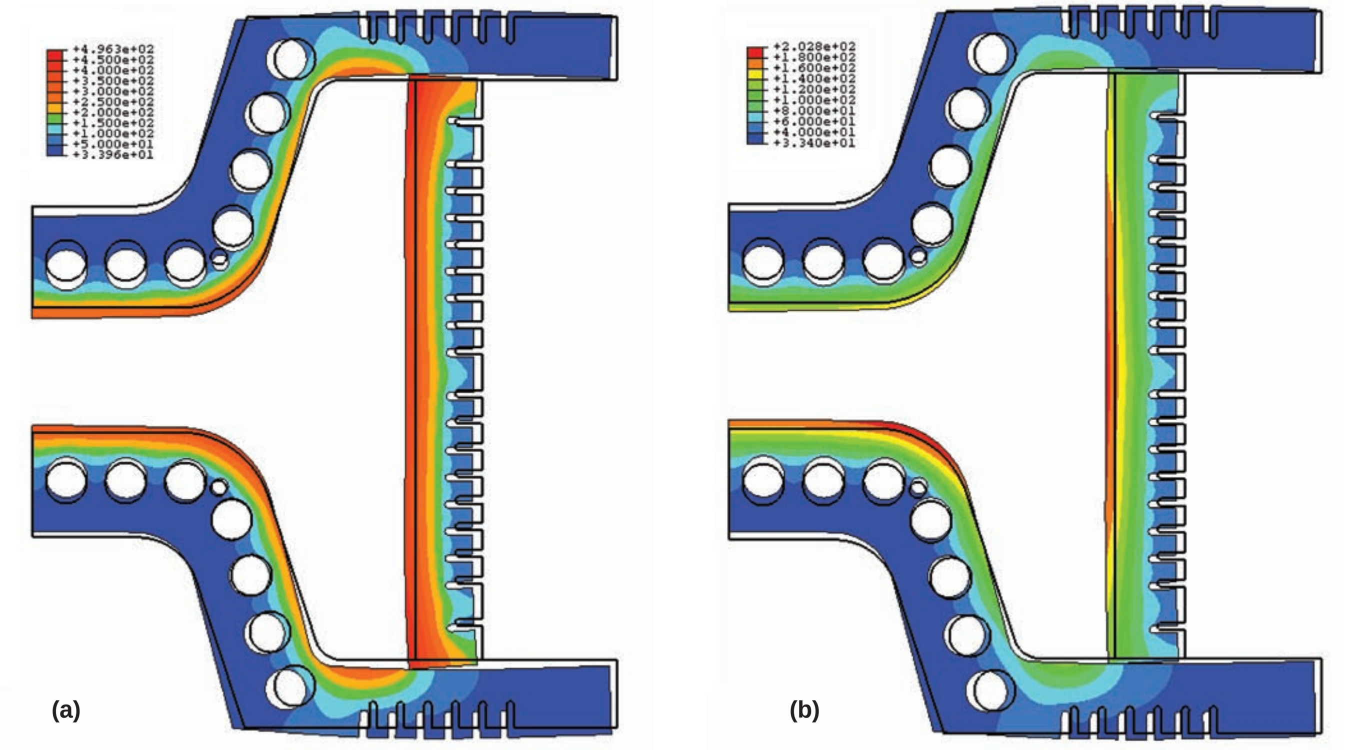

Predicted mold temperatures with slice model at (a) the meniscus and (b) midway down the mold.

mold heat flux from the temperature increase of the cooling water. Figure 9 shows typical results from the model. Note that the inside radius (bottom of Figure 9b) has higher hot face temperatures, owing to the thicker copper plates midway down the mold from the mold curvature.

Figures 10 and 11 show the agreement obtained between the model predictions at the thermocouple (TC) locations and the thermocouple measurements after adjustment to take into account a 0.01-mm air gap on the wide face. The adjustment calculation was performed by assuming the thermocouple acts like a rod-fin, with a heat transfer coefficient of 60 Wm^{-2} K^{-1} (air for most thermocouples) and 3 kWm^{-2} K^{-1} (average value for air and water environment experienced by thermocouple wire that passes through the wide face water slot near the shoulder TC B). Note that the thermocouples on the wide faces all give low values prior to adjustment. The presence of even this tiny air gap is enough to greatly change the results. After adjustment, the measurements roughly match or exceed the numerical predictions. The following equation is used to calculate the adjusted temperature:

$$T_{adjusted} = T_{measured} + \frac{\left(T_{measured} - T_{\infty}\right)\Delta x \sqrt{h\pi D k_{TC}}}{\sqrt{\pi} k_{air} D / 2} \qquad \text{(Eq. 9)}$$

where

D = 3.175 mm is the diameter of thermocouple wire,

k_{TC} = 19.2 W/m·K for chromel-slumel thermocouples,

T_{∞} = 25°C is the ambient temperature and

k_{air} = 0.026 W/m·K and $\Delta x \approx$ 0.01 mm is the approximate gap thickness.

Figure 10

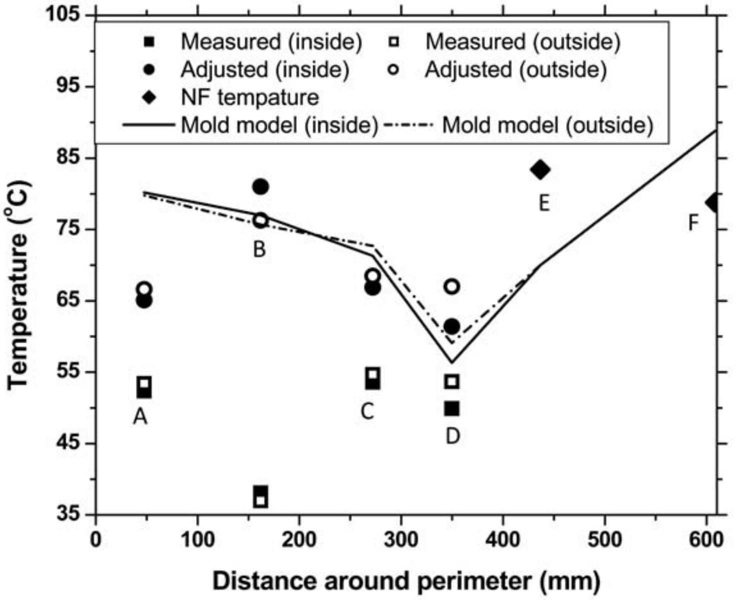

Comparison of temperature for a transverse slice (590.6 mm below mold top).

Figure 11

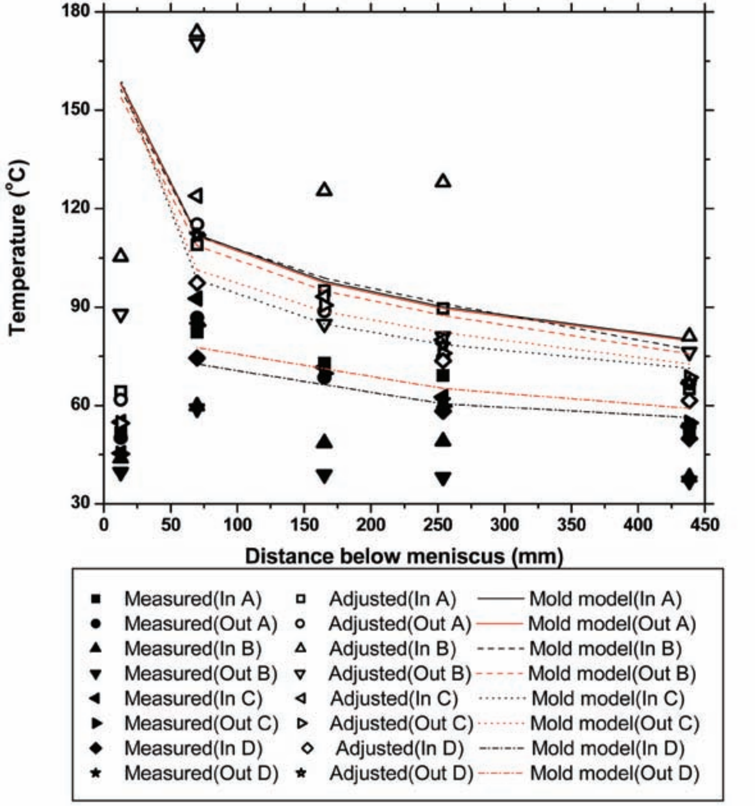

Comparison of temperature down mold wide face.

Mold Thermal Distortion Model

A full 3-D finite element model of one-fourth of the mold and water box was constructed to accurately calculate mold temperature and mold distortion. Much of the actual detail of the mold geometry was included in the model, such as the casting radius on the hot face, water channels and bolt holes. The calculated mold temperatures shown in Figure 12 are the result of the same calibrated heat flux profiles used in the shell model and the mold slice model, presented in the next section. Figure 13 shows the surface temperature profiles down the mold at a few points around the perimeter. The warmest place on the wide face is at the shoulder, due to convergent heat flow into the mold, agreeing with previous work by Thomas et al.[10] The temperatures increase locally at the bottom of the mold because the water channels do not run the entire length of the mold. Figures 14 and 15 show temperature and distortion profiles of two horizontal slices through the mold.

Model of Solidifying Steel Shell

The coupled two-dimensional transient model of thermal-mechanical behavior of the solidifying steel shell moving down the contoured surface of the mold was applied to simulate temperature, solidified shell thickness growth, deformation and stress in the shell, in addition to interfacial heat flux and gap formation between the shell and the mold. The simulation results presented here included mold taper, but did not include the 3-D mold distortion shape.

Heat Flux — The heat flux around the perimeter for several horizontal slices of the mold is shown in Figure 16, and the heat flux profiles down the mold for multiple points around the

Figure 12

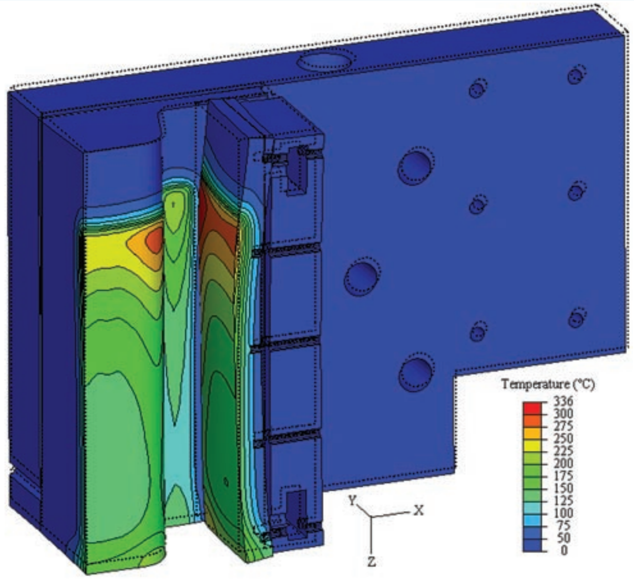

3-D mold temperature results (distortion magnified 20x).

Figure 13

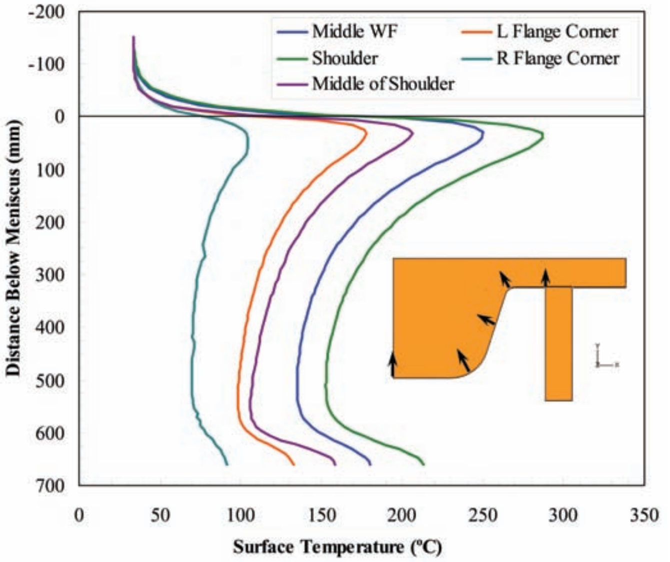

Temperature profiles down the mold.

Figure 14

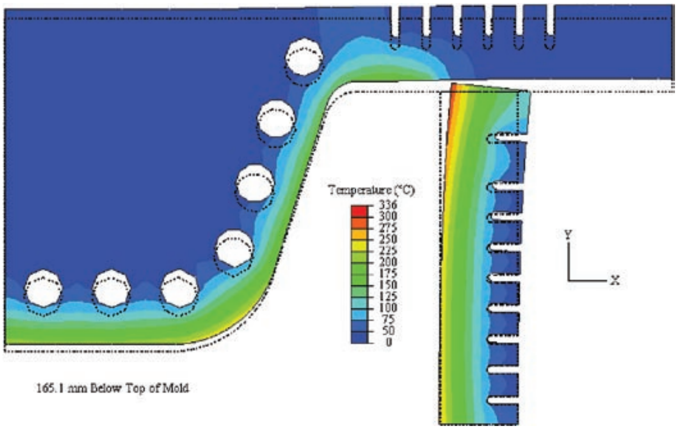

Temperature results at 165.1 mm below mold top (distortion magnified 10x).

Figure 15

Temperature results at 406.4 mm below mold top (distortion magnified 10x).

perimeter are presented in Figure 17. The average values for the narrow face and wide face are almost the same because these profiles are computed using the coupled model for gap heat conduction (Equation 5), but the wide face removes more heat, owing to its larger perimeter. The model overpredicts the total heat flux in the mold by about 4%, which can be attributed to the greater overprediction of the wide face balancing the underprediciton of the narrow face, as shown in Table 3.

Matching the heat flux in both of the mold and shell models with the measurements based on heat-up of the cooling water is a difficult task, because the interfacial gaps are not known *a priori*. Manual iteration between the different models was required.

Table 3

Comparison of Predicted and Measured Mold Heat Flux

	Experimental	Mold model	Error
Wide face	1,112.4 kW	1,204.7 kW	+8.30%
Narrow face	651.4 kW	634.2 kW	−2.64%
Total	1,763.8 kW	1,838.9 kW	+4.26%

Shell Behavior — Figure 18 shows typical contours of the solidus, liquids, and 30% solid temperature about midway down the mold. Temperature profiles through the shell thickness are shown in Figure 19 at an important location: the shoulder. The shell becomes slightly thinner and hotter at the end of the shoulder region, owing to the drop in heat flux experienced

Figure 16

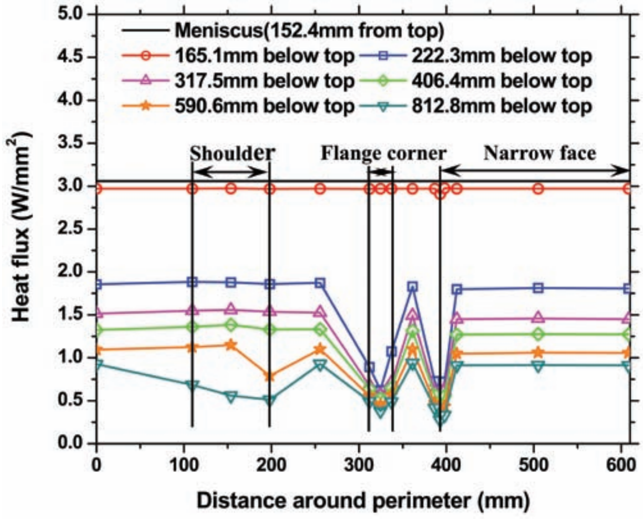

Heat flux around the perimeter.

Figure 17

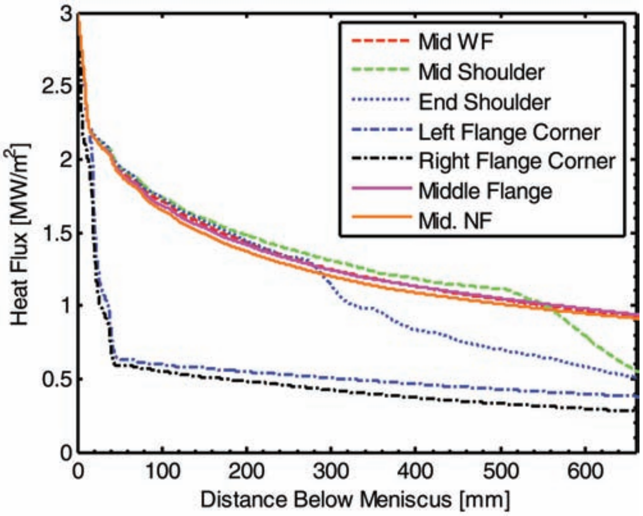

Heat flux down the mold at points around the perimeter.

Figure 18

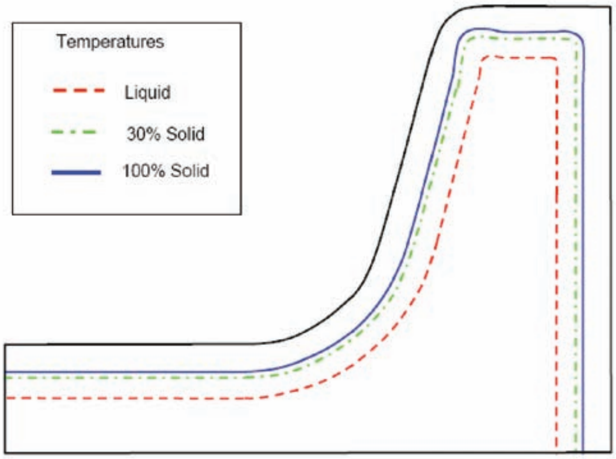

Major temperature contours (457 mm below meniscus).

Figure 19

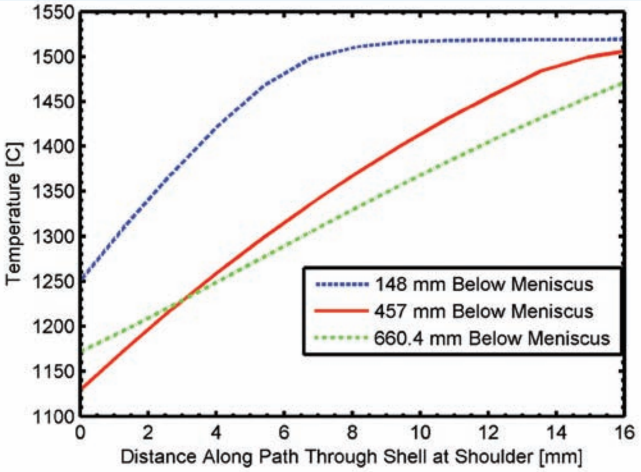

Temperature profile through shell thickness at shoulder.

there at lower distances, as shown in Figures 16 and 17. This is due to the formation of an air gap in this region, which arises because there is too much taper at the shoulder. The shell does not shrink enough, so it buckles away from the mold wall in this region. This is pictured in Figure 20. Lower in the mold, a second gap opens up in the middle of the shoulder. This influence of excessive taper on the shoulder region is opposite to the effect that excessive taper would have in the corners, owing to the convex shape of the mold in this region.

The shell also becomes thinner at the left flange corner for the same reasons. The gap pictured in Figure 21 coincides with the drop in heat flux in Figures 16 and 17, and the thinner shell in Figure 18. This result shows that air gap formation is far more influential on heat transfer than the effects of two-dimensional conduction, which tends to increase cooling of the corners slightly.

The evolution of temperature and gap size at seven points around the shell perimeter is presented in Figures 22 and 23. Their locations are labeled in Figure 4. The heat flux that leaves the shell surface for these seven points is given in Figure 17. Most of the perimeter — including the middle of the wide face, narrow face and middle of the flange — stays in touch with the mold all the time, so the heat flux and temperature histories at these points are fairly uniform with no large jumps or gaps. Both flange corner points shrink away from the mold, increasing gap heat resistance, dropping heat flux and increasing shell temperature. The shoulder region also forms gaps, as discussed earlier, which drops local heat extraction and increases temperature. In fact, excessive reheating and thinning of the shell at this location resulted in a breakout at the shoulder region after exiting the mold.

Figure 20

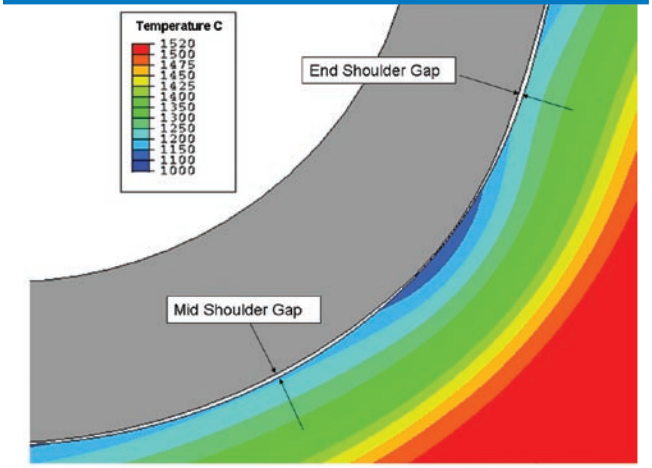

Shoulder shell temperature contours with gap detail at 457 mm below meniscus.

Figure 21

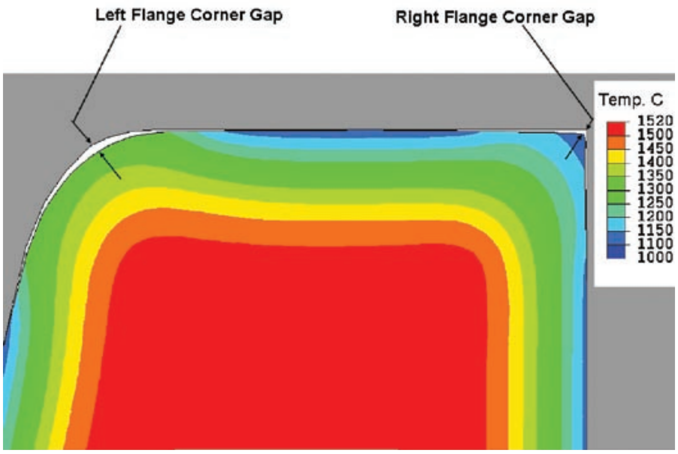

Flange shell temperature contours with gap details at 457 mm below meniscus (1x magnification).

Figure 22

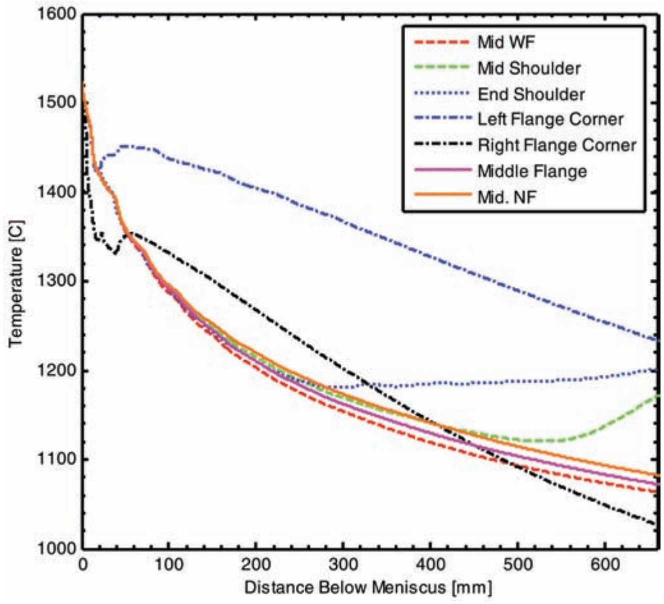

Temperature histories for the points on the shell perimeter.

Figure 23

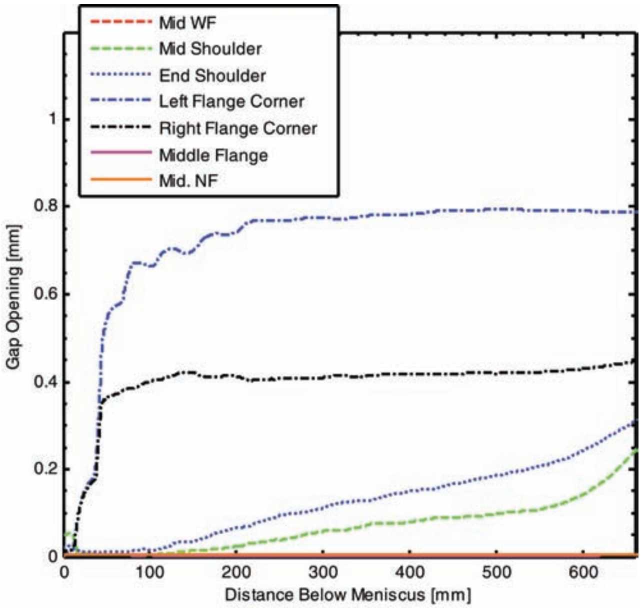

Gap histories for the points on the shell perimeter.

The maximum principal stress contours midway down the mold are given in Figure 24. They reveal the expected tensile stress peaks just past the solidification front. These are seen more clearly in Figure 25, where hoop stress is the stress component tangential to the mold wall. This is where hot tear cracks are most likely to form, owing to the combined effects of this stress and metallurgical embrittlement caused by liquid films from microsegregation. Although the stress is only a few MPa, the strains are more significant. These stress results are consistent with the results of the validation test problem, where surface shell compression and sub-surface shell tension close to the solidification front are revealed. The largest stresses are found in the shoulder region, which is consistent with where shell failure starts, leading to the breakout.

As the solidification progresses, the faster cooling of the interior relative to the surface region naturally causes more interior contraction and tensile stress, along with more compression at the surface. This is why hoop stress in Figure 25 increases with distance down the mold. Additional stress may be due to mechanical bending caused by the middle of the flange pushing on the shell.

Shell Thickness Validation — Shell thickness at 30% solid predicted by the model is

Figure 24

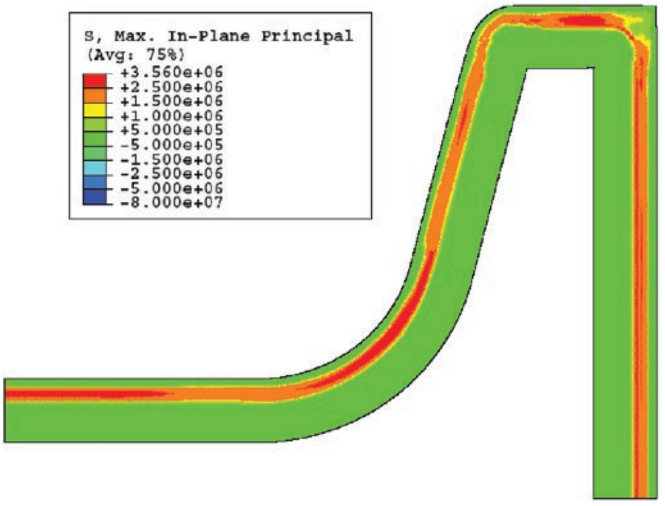

Maximum principal stress contours 457 mm below meniscus.

Figure 25

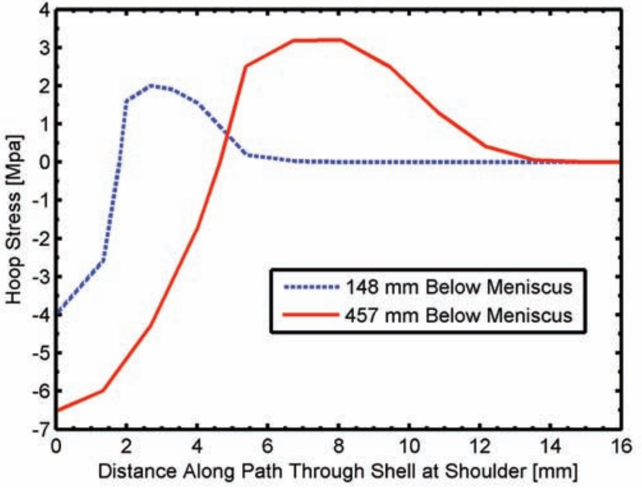

Hoop stress along the path through shell thickness at the shoulder.

Figure 26

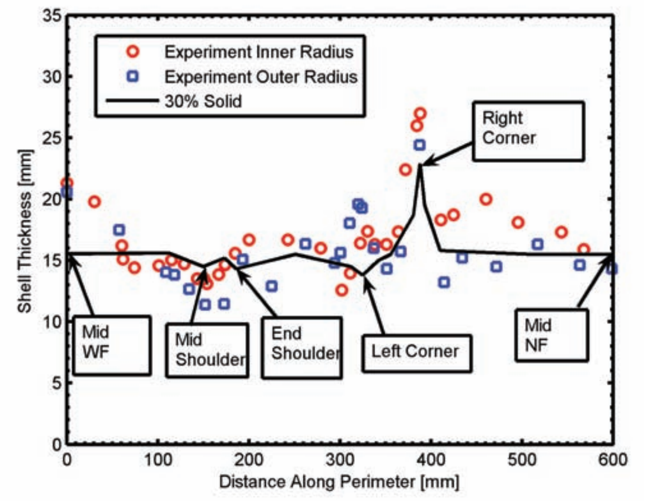

Shell thickness comparisons at 457 mm below meniscus.

Figure 27

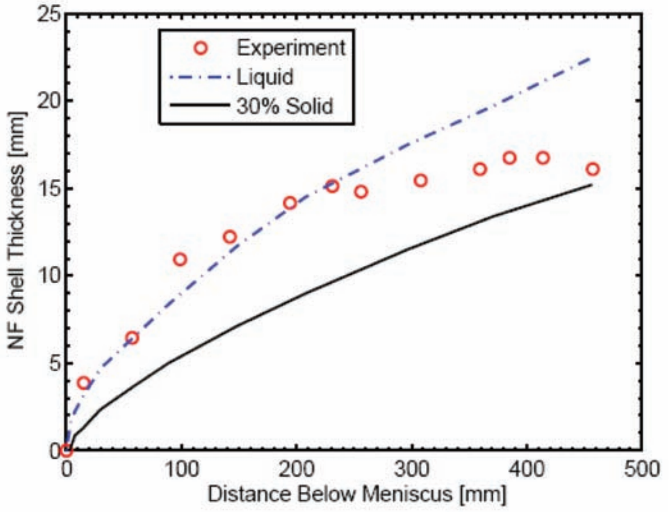

Shell thickness history for a point on the narrow face 50 mm from the corner.

compared with measurements around the perimeter of the breakout shell in Figure 26. A reasonable match is observed everywhere except the middle portion of the wide face (web), where the measured shell appears to be 5 mm thicker. This is likely caused by the uneven superheat distribution due to the flow pattern in the liquid pool,[5] as this location is farthest away from the pouring funnels. Superheat variations are not included in the model. The measured thickness profile down the shell for a point on the narrow face 50 mm from the corner is compared with the model predictions in Figure 27.

Conclusions

A coupled thermal-mechanical model of continuous casting of steel is applied to accurately simulate the continuous casting of steel beam blanks and is validated with plant measurements. The model features an efficient local-global numerical procedure to integrate a realistic elastic-viscoplastic phase-dependent constitutive model that has been implemented into the commercial package ABAQUS. The model is first validated with a semi-analytical solution of thermal stress in an infinite solidifying plate. The model is then applied to simulate temperature, strain and stress in a one-quarter transverse section of a commercial beam blank caster with realistic complex geometry, temperature-dependent material properties, and operating conditions. The results compare well with in-plant measurements of temperature from thermocouples embedded in the beam blank mold walls, total heat flux from a heat balance on the cooling water temperature rise, and the thickness of the solidifying shell measured after a breakout. The model provides valuable insights into the mechanisms of shoulder shell failure triggered initially by a thinner shell under combined thermomechanical stress conditions, and later accelerated by a shoulder gap opening. This model is ready to be applied in future parametric studies of optimum taper and slag film thickness solutions that will minimize the amount of failures and maximize the productivity of continuous beam blank casting.

Acknowledgments

The authors would like to thank the Steel Dynamics Structural and Rail Mill for their great support for this project, and the National Center for Supercomputing Applications (NCSA) from computational and software resources. Support of this work by the Continuous Casting Consortium at the University of Illinois and the National Science Foundation Grant # DMI 05-28668 is gratefully acknowledged.

References

1. ABAQUS Inc., ABAQUS Standard User Manuals v6.6, Providence, R.I., 2007.

2. S. Koric and B.G. Thomas, "Efficient Thermo-Mechanical Model for Solidification Processes," *Inter. Journal for Numerical Methods in Eng.*, 2006, Vol. 66, pp. 1955–1989.

3. S. Koric, Ph.D. thesis, University of Illinois, 2006.

4. J.H. Weiner and B.A. Boley, "Elasto-plastic Thermal Stresses in a Solidifying Body," *J. Mech. Phys. Solids,* 1963, Vol. 11, pp. 145–154.

5. C. Li and B.G. Thomas, "Thermomechanical Finite-Element Model of Shell Behavior in Continuous Casting of Steel," *Metal. & Material Trans. B.*, 2004, Vol. 35B (6), pp. 1151–1172.

6. H. Zhu, Ph.D. thesis, University of Illinois, 1993.

7. B.G. Thomas and C. Ojeda, "Ideal Taper Prediction for Slab Casting," *Manfred Wolf Memorial Symposium Proceedings,* ISS-AIME, Warrendale, Pa., 2003, pp. 295–308.

8. C. Li and B.G.Thomas, "Maximum Casting Speed for Continuous Cast Steel Billets Based on Sub-Mold Bulging Computation," *Steelmaking Conf. Proc*., AIST, Warrendale, Pa., 2003, Vol. 86.

9. J. Lait., J.K. Brimacombe and F. Weinberg, "Mathematical Modelling of Heat Flow in the Continuous Casting of Steel," *Ironmaking and Steelmaking*, 1974, Vol. 2, pp. 90–98.

10. B.G. Thomas, J. Jiang and D. Lorento, "Optimization of Water Channel Design in Beam Blank Molds," *5th European Continuous Casting Conf*. (Nice, France, June 20–22, 2005), The Institute of Materials, Minerals & Mining, Paris, 2005, Vol. S16 3, pp. 139–147.

11. F. Leingruber, C. Chimani, M. Thalhammer and G. Shan, *CCR04 Conference* (Linz, Austria), VAI Technology, Linz, Austria, 2004, Vol. 4.1, pp. 1–9.

12. J.-E. Lee, T.-J. Yeo, K.H. Oh, J.-K. Yoon and U.-S. Yoon, "Prediction of Cracks in Continuously Cast Steel Beam Blank Through Fully Coupled Analysis of Fluid Flow, Heat Transfer, and Deformation Behavior of a Solidifying Shell," *Metal. and Material Trans. A,* 2000, Vol. 31A (1), pp. 225–237.

13. J.O. Kristiansson, "Thermomechanical Behavior of the Solidifying Shell Within Continuous-Casting Billet Molds — A Numerical Approach," *Journal of Thermal Stresses,* 1984, pp. 209–226.

14. J.M. Risso, A.E. Huespe and A. Cardona, "Thermal Stress Evaluation in the Steel Continuous Casting Process," *Intl. Journal for Numerical Methods in Eng*., 2006, Vol. 65(9), pp. 1355–1377.

15. P.F. Kozlowski, B.G. Thomas, J.A. Azzi and H. Wang, "Simple Constitutive Equations for Steel at High Temperature," *Metal. & Material Trans. A,* 1992, Vol. 23A, pp. 903–918.

16. Ansys Inc., Ansys User Manuals, v10, Canonsburg, Pa., 2006.

17. A.M. Lush, G. Weber and L. Anand, "An Implicit Time-Integration Procedure for a Set of Internal Variable Constitutive Equations for Isotropic Elasto-Viscoplasticity," *International Journal of Plasticity,* 1989, Vol. 5, pp. 521–549.

18. M.A. Crisfiled, *Nonlinear FEA of Solids and Structures*, Wiley, 1991.

19. O.C. Zienkiewicz and R.L. Taylor, *Finite Element Method: Solid and Fluid Mechanics Dynamics and Non-Linearity,* McGraw-Hill, 1991.

20. J.C. Simo and R.L. Taylor, *Computer Methods in Applied Mechanics and Eng*., 1985, Vol. 48, pp. 101–118.

21. P.J. Wray, "Effect of Carbon Content on the Plastic Flow of Plain Carbon Steels at Elevated Temperatures," *Metal. Trans. A,* 1982, Vol. 13, pp. 125–134.

22. T. Suzuki, K.H. Take, K. Wunnenberg and K. Schwerdtfeger, "Creep Properties of Steel at Continuous Casting Temperatures," *Ironmaking and Steelmaking,* 1988, Vol. 15, pp. 90–100.

23. J.K. Park, B.G. Thomas and I. Samarasekera, "Analysis of Thermo-Mechanical Behavior in Billet Casting With Different Mold Corner Radii," *Ironmaking and Steelmaking,* 2002, Vol. 29(5), pp. 359–375.

24. H.N. Han, J.E. Lee, T.J. Yeo, Y.M. Won, K. Kim, K.H. Oh and J.K. Yoon, "A Finite Element Model for 2-Dimensional Slice of Cast Strand," *ISIJ International,* 1999, Vol. 39(5), pp. 445–455.

25. Y.-M. Won and B.G. Thomas, "Simple Model of Microsegregation During Solidification of Steels," *Metal. and Material Trans. A,* 2001, Vol. 32A, No. 7, pp. 1755–1767.

26. Y. Meng and B.G. Thomas, "Heat Transfer and Solidification Model of Continuous Slab Casting: CON1D," *Metal. and Material Trans. B,* Vol. 34B, No. 5, Oct. 2003, pp. 685–705.

◆

This paper was presented at AISTech 2008 — The Iron & Steel Technology Conference and Exposition, Pittsburgh, Pa., and published in the Conference Proceedings.